# Advanced Wireless Power and Data Transmission Techniques for Implantable Medical Devices

Hyung-Min Lee, *Member, IEEE*, Mehdi Kiani, *Member, IEEE*, and Maysam Ghovanloo, *Senior Member, IEEE*

School of Electrical and Computer Engineering, Georgia Institute of Technology, Atlanta, GA

***Abstract*—Short-range wireless power and data transmission offers a viable mean to power up implantable medical devices (IMDs) with a wide range of power levels and communicate with external units across the skin. To optimize wireless power transfer (WPT), it is key to improve efficiencies in every stage of the power delivery path from external power sources to the IMD, while maintaining robustness and safety against load variations, coil misalignments, and nearby conductive objects. This paper reviews various mechanisms for WPT with focus on link structures and circuit techniques for wirelessly-powered IMDs. Moreover, advanced IMDs require wireless data telemetry (WDT) for wideband bidirectional data communication in the presence of the strong power carrier interference. This paper also discusses several modulation schemes and transceiver circuits for low-power, carrier-less, and robust WDT.**

## I. Introduction

Wireless power transfer (WPT) is one of the few viable methods to power up implantable medical devices (IMDs) or recharge IMD batteries across the skin without direct electrical contacts. There are several IMD applications with various power requirements such as microwatts in neural sensors, milliwatts in neural stimulators and cochlear implants, and watts in artificial hearts [1]. High power transfer efficiency (PTE), robustness against load variations, nearby objects, and coil misalignments, and extended power transfer range are highly desired in all of these applications.

More recent IMDs demand higher performance to enable sophisticated treatment paradigms, such as retinal implants for the blind or bidirectional cortical brain-computer-interfacing (BCI) with sensory feedback for amputees or those suffering from severe paralysis [2], [3]. These IMDs require higher power to handle more functions on a larger scale under variable environmental effects and loading conditions. Particularly when stimulation is needed through a large number of electrodes at high rates, power level is inherently high and less dependent on the power consumption of internal circuits [4]. Therefore, the power consumption of the new IMDs is going to be at least an order of magnitude higher than the traditional IMDs, such as pacemakers [5]. As such, achieving higher PTE becomes essential to keep the temperature rise with strict safety limits [6]. In most cases, supplying IMDs with primary batteries will not be an option because of their large volume, limited lifetime, replacement hardship, and cost [7].

This work was supported in part by the National Institute of Biomedical Imaging and Bioengineering grant 1R21EB018561 and the National Science Foundation under awards IIP-1439426, ECCS-1407880, and ECCS-1408318.

Hyung-Min Lee is currently with Department of Electrical Engineering and Computer Science, Massachusetts Institute of Technology, Cambridge, MA 02139, USA.

Mehdi Kiani is currently with Department of Electrical Engineering, the Pennsylvania State University, University Park, PA 16802, USA.

Maysam Ghovanloo* is with the GT-Bionics lab, School of Electrical and Computer Engineering, Georgia Institute of Technology, Atlanta, GA 30308, USA (phone: 404-385-7048; fax: 404-894-4701, email: mgh@gatech.edu).

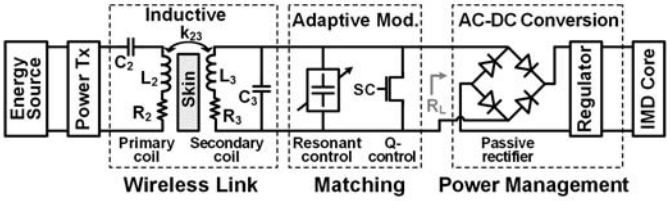


Fig. 1. Generic wirelessly-powered IMD structure with emphasis on key blocks for efficient WPT.

Figure 1 shows the block diagram of a generic wirelessly-powered IMD with emphasis on key blocks for efficient WPT: the transcutaneous power is commonly delivered through an inductive link, matching circuit, and power management unit. A power transmitter (Tx), which is supplied by an external energy source, drives the primary coil, $L_2$, at the power carrier frequency, $f_p$. An AC signal is induced across the secondary coil, $L_3$, because of the coils' electromagnetic flux coupling. The receiver (Rx) resonance circuit, $L_3C_3$-tank, boosts the AC voltage, while the matching circuit adaptively optimizes the link resonance and quality ($Q$) factor against the surrounding tissue parasitic, coil coupling, and IMD loading variations. The $L_3C_3$-tank is followed by the power management unit for AC-DC conversion and voltage regulation to supply the rest of the IMD. The power management circuitry and the IMD core in Fig. 1 have been modeled as an AC resistance, $R_L$, in this paper.

Considering power losses at each stage of the power delivery path, the total PTE, $\eta_{Total}$, from the external energy source to the IMD core can be calculated as,

$$\eta_{Total} = \eta_{TX} \times \eta_{L2} \times \eta_{Skin} \times \eta_{L3} \times \eta_{PMU}, \quad (1)$$

where $\eta_{TX}$, $\eta_{L2}$, $\eta_{Skin}$, $\eta_{L3}$ and $\eta_{PMU}$ are efficiencies of the power Tx, primary LC-tank, transcutaneous powering through skin, secondary LC-tank, and power management unit, respectively. The wireless link efficiency, $\eta_{Link}$, can be represented as $\eta_{L2} \times \eta_{Skin} \times \eta_{L3}$, while $\eta_{PMU}$ typically includes efficiencies of the AC-DC converter (e.g. rectifier) and regulator.

Achieving higher overall PTE ($\eta_{Total}$) is very important in wirelessly-powered IMD applications because it allows them to operate with smaller received power from a larger coil distance. Moreover, lower transmitted power reduces the risk of tissue damage from overheating and interference with other devices [8]. In the IMD applications, the transmitted power level and link efficiency ($\eta_{Link}$) are typically limited due to the energy

absorption in the skin and the size constraint of the implanted secondary coil ($L_3$). Therefore, various WPT techniques should be adopted in every stage of the power flow, particularly across the skin (wireless link) and inside the skin (matching and PMU in IMDs) to efficiently deliver as much energy as possible to the target IMD. This also improves the overall PTE, WPT range, low temperature operation, and robustness.

In addition to WPT, wireless data telemetry (WDT) is one of the most important functions in a group of IMDs, particularly for neuroprostheses that substitute sensory or motor modalities that are lost due to an injury or a disease. Well-known examples are the cochlear implants and visual prostheses, which need a large volume of data from external sensors to the IMD [9]. Another example is invasive brain-computer interfaces, which collect a massive amount of data from the central neural system and transfer it to the outside of body to control the patient's environment or prosthetic limbs after signal processing [10].

In these IMDs, high-bandwidth WDT must be achieved at the lowest possible carrier frequencies because of significant electromagnetic-field absorption in the tissue, which increases exponentially with the carrier frequency [11]. This requirement rules out the majority of commercially-available wideband wireless protocols, such as Bluetooth or WiFi, which operate at 2.4 GHz. There are also specific standards, such as Medical Implant Communication Service (MICS), operating in the 402 - 405 MHz band, which can only offer a limited bandwidth (300 kHz) [12]. Therefore, utilizing a pair of loosely-coupled coils is the most common method for establishing wideband WDT in IMDs. Achieving low-power consumption, small size, and wide bandwidth as well as maintaining robustness against external interferences, relative distance variations, and coil misalignments are major challenges in establishing WDT links.

In this paper, we review various WPT schemes with focus on wireless link mechanisms and circuit techniques for matching and power management units in IMD applications. We also explore recent WDT techniques that enable wideband and robust data telemetry between IMDs and external units. Section II introduces several wireless link mechanisms and their adaptive matching techniques. Section III presents various power conversion/management circuits in IMDs, such as AC-DC converters, regulators, and chargers. Section IV discusses recent WDT techniques for low-power telemetry with IMDs, followed by conclusions in Section V.

## II. Optimized Wireless Power Transfer Links

### A. Three-Coil Inductive Links

Figure 1 shows WPT via a conventional 2-coil inductive link, in which both LC-tanks are tuned at $f_p$. The inductive link PTE is mainly dependent on the mutual coupling between the coils, $k_{23}$, and their quality factors, $Q_2 = \omega L_2/R_2$ and $Q_3 = \omega L_3/R_3$, which all depend on the geometries of $L_2$ and $L_3$ coils. The link PTE can be found from,

$$\eta_{2-coil} = \frac{k_{23}^2 Q_2 Q_{3L}}{1 + k_{23}^2 Q_2 Q_{3L}} \cdot \frac{Q_{3L}}{Q_L}, \quad (2)$$

where $Q_L = R_L/\omega L_3$ is often referred to as the load quality factor, $Q_{3L} = Q_3 Q_L/(Q_3+Q_L)$, and the first and second terms represent the power loss in $R_2$ and $R_3$, respectively [13]. It can be seen from (2) that large $k_{23}$, $Q_2$, and $Q_3$ are needed to maximize the PTE. However, for a given set of $Q_2$, $Q_3$, and $k_{23}$ values, there is an optimal load, $R_{L,PTE} = \omega L_3 Q_{L,PTE}$, which can maximize the PTE. $Q_{L,PTE}$ can be found from,

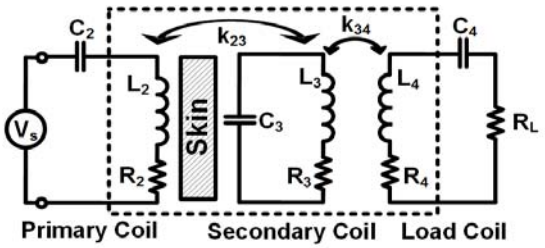


Fig. 2. Lumped circuit model of the 3-coil inductive link with two coils in the IMD side to improve the PTE by $R_L$ transformation [16].

$$Q_{L,PTE} = \frac{Q_3}{(1 + k_{23}^2 Q_2 Q_3)^{1/2}}. \quad (3)$$

The $R_L$ value, which depends on the IMD power consumption, is usually defined by the application. Therefore, the 2-coil links might not achieve the optimal $Q_{L,PTE}$ in (3) for a given $R_L$.

The magnetic resonance-based power transmission in the form of a 3-coil inductive link has been proposed to maximize the PTE for a certain $R_L$ by performing impedance transformation [14]-[17]. The 3-coil link, shown in Fig. 2, adds a new degree of freedom ($k_{34}$) compared to its 2-coil counterpart by adding load $L_4$ coil. This can transform any given $R_L$ to the optimal load in (3), which is required to achieve high PTE in the loosely-coupled $L_2$-$L_3$ link. The PTE of the 3-coil link can be found from,

$$\eta_{3-coil} = \frac{(k_{23}^2 Q_2 Q_3)(k_{34}^2 Q_3 Q_{4L})}{[(1 + k_{23}^2 Q_2 Q_3 + k_{34}^2 Q_3 Q_{4L})(1 + k_{34}^2 Q_3 Q_{4L})]} \cdot \frac{Q_{4L}}{Q_L}, \quad (4)$$

where $k_{24}$ has been safely neglected in comparison to coupling coefficients between neighboring coils ($k_{23}$ and $k_{34}$) [16]. For a certain $R_L$, the optimal choice of $k_{34}$ that maximizes the PTE of the 3-coil inductive link can be found from,

$$k_{34,PTE} = \left( \frac{1 + k_{23}^2 Q_2 Q_3}{Q_3^2 Q_{4L}^2} \right)^{1/4} = \left( \frac{\left(1 + k_{23}^2 Q_2 Q_3\right)\left(1 + R_L/R_4\right)^2}{Q_3^2 Q_4^2} \right)^{1/4}. \quad (5)$$

Figure 3 compares the PTEs of 2- and 3-coil links vs. $R_L$ for a design example in [16]. Since the optimal $Q_{L,PTE}$ in the 3-coil link is adjustable with $k_{34}$ based on (5), the optimal PTE has been maintained for the 3-coil link in a wide range of $R_L$ (10 Ω ~ 1 kΩ). However, with a 2-coil link the optimal PTE has been achieved only for a specific $R_{L,PTE}$ = 200 Ω that satisfies (3). It should be noted that at small coupling distances ($d_{23}$), where $k_{23}$ is relatively large, the 2-coil link requires smaller $Q_{L,PTE}$ in (3), which is relatively easy to achieve. Therefore, for short distance inductive power transmission, which is the case in most transcutaneous IMD applications, the conventional 2-coil inductive link that is properly designed can be very close to the optimal choice [16].

### B. Adaptive Matching Techniques

The problems with 3-coil links are that they add an additional coil in the Rx, which adds to the size and cost of the IMD, and more importantly they cannot dynamically compensate for $R_L$ variations during the operation. In IMDs, $R_L$ can change during the operation while the optimal $k_{34}$ in (5), which depends on the geometries of $L_3$ and $L_4$ and their relative distance ($d_{34}$), can

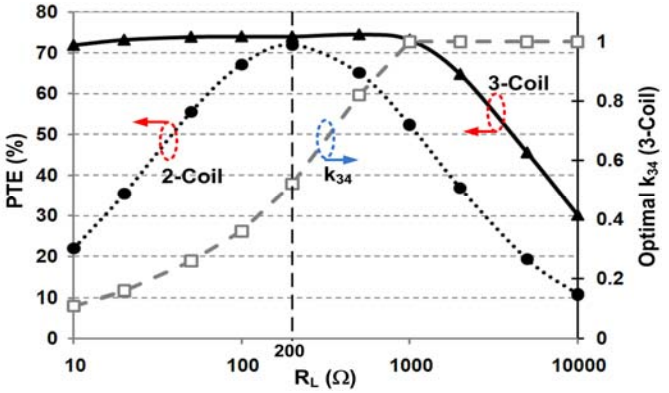


Fig. 3. The PTE comparison between 2- and 3-coil links vs. $R_L$ showing that by $k_{34}$ adjustment, the optimal PTE can be maintained in the 3-coil link [17].

only be adjusted during the design and IMD fabrication.

As an alternative to the 3-coil link, several groups have suggested to use off-chip matching circuits to transform $R_L$ [18]-[20]. Different types of matching networks such as π, T, and L can be designed for inductive links. In order to achieve high PTE, the L-match network has mostly been implemented for inductive links in the past by only using one inductor and one capacitor at the output of the $L_3C_3$-tank in Fig. 1. In practice with $R_L$ variations during the operation, a network of switched capacitors and inductors, which are often off-chip due to the low-frequency operation of inductive links (MHz and below), is required to dynamically transform $R_L$, which again adds to the size, cost, and power loss in the IMD.

These dynamic matching issues involved in the use of 3-coil links and matching circuits have been the motivation behind the Q-modulation technique for adaptive and efficient inductive power transmission when $R_L$ varies significantly during the operation [21]. In the Q-modulation inductive link shown in Fig. 4a, the current in the series $L_3C_3$-tank ($I_3$) is sampled, and a switch (SC) shorts the $L_3C_3$-tank for the duration of $T_{on}$ at the zero-crossing times of $I_3$ once in every half-cycle of the power carrier ($T_p = 1/f_p$). As shown in the switching diagram of Fig. 4b, by closing SC during $\Phi_1$ and therefore shorting $R_L$, the high-Q $L_3C_3$-tank stores the maximum energy (proportional to $I_3$), that can be transferred from Tx. During $\Phi_2$, SC is opened and the $L_3C_3$-tank is connected to $R_L$ to deliver its stored energy. Therefore, $Q_{3L}$ and the amount of the transferred energy to $R_L$ can be controlled by the duty cycle of the switching waveform, i.e. $D = 2T_{on}/T_p$.

The equivalent $Q_{3L}$ of the switched $L_3C_3$-tank in Fig. 4a can be found by calculating the ratio of the stored energy inside the $L_3C_3$-tank to the average power dissipation of the secondary side in the steady state,

$$Q_{3L,eq} = \frac{\omega_p L_3}{R_3 + R_{sw}\left[D - \sin(2\pi D)/2\pi\right] + R_L\left[1 - D + \sin(2\pi D)/2\pi\right]} \quad (6)$$

where $R_{sw}$ is the switch resistance [21]. It can be seen from (6) that when $D$ increases from 0% (i.e. no Q-modulation) when only $R_L$ is connected to the $L_3C_3$-tank to 100%, when only $R_{sw}$ is connected to the $L_3C_3$-tank, $Q_{3L,eq}$ is improved from $\omega_p L_3/(R_3+R_L)$ to $\omega_p L_3/(R_3+R_{sw})$. Thus, $D$ can be adjusted dynamically during the WPT operation to achieve the optimal $Q_{L,PTE}$ in (3), in the presence of $R_L$ variations.

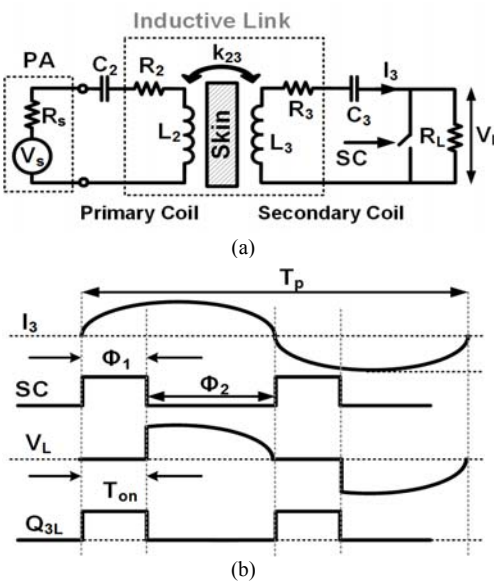


Fig. 4. (a) A Q-modulation inductive link for dynamic transformation of $R_L$, and (b) the switching waveforms to control $Q_{3L}$ by adjusting $D = 2T_{on}/T_p$ [21].

## III. Power Conversion and Management Circuits

Various power conversion and management topologies can be used following the WPT link: AC-DC converters, regulators, and battery/capacitor chargers. The choice of power conversion structure depends on design specifications, such as operating frequency, power conversion efficiency (PCE), peak input voltage, dropout voltage, delivered power capacity, and size. The PCE of the AC-DC converter is a key factor in improving the overall power efficiency of IMDs because the entire received power from the wireless link needs to pass through this block. Since AC-DC output voltage changes with coil distance variations and misalignments, a low-dropout regulator (LDO) often follows the AC-DC converter to provide constant supply voltage to the IMD.

### A. Active AC-DC Converters

Passive AC-DC converters have simple structures using diode-connected transistors. However, they suffer from large voltage dropout and power loss because of MOSFET threshold voltages ($V_{TH}$), resulting in low PCE [22], [23]. Several $V_{TH}$-compensation techniques have been proposed to reduce the forward voltage drop by adjusting effective $V_{TH}$ in passive AC-DC converters [24], [25]. However, they still suffer from issues such as sensitivity to process variations, leakage, and reverse currents.

In order to increase the PCE further by decreasing transistor dropout voltage, comparator-based active AC-DC converters with synchronous switches are considered the most promising solutions [26]-[28]. Figure 5 shows the block diagram of an active voltage doubler employing active diodes in which main switches ($N_1$ and $P_1$) are driven by high-speed comparators ($CMP_N$ and $CMP_P$) [28]. $CMP_N$ compares $V_{VD}$ with $V_{SS}$ and controls the switching of $N_1$. When $V_{VD} < V_{SS}$, $CMP_N$ output goes high, $N_1$ turns on with a low dropout voltage, $V_{DS(N1)}$, and $C_{IN}$ is charged to $V_{IN,peak}$ - $V_{DS(N1)}$. Similarly, when $V_{VD} > V_{OUT}$, $CMP_P$ output goes low, $P_1$ turns on with a low dropout voltage, $V_{SD(P1)}$, and charging current flows through a low-resistance path to charge the load, $R_OC_O$. Therefore, after a few cycles,

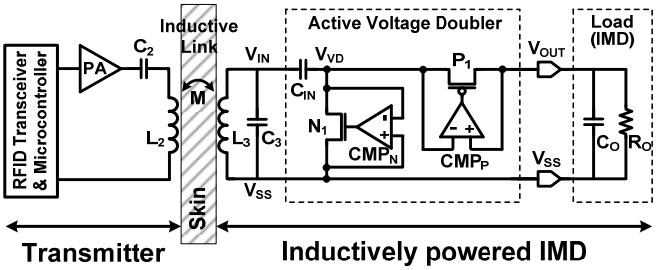


Fig. 5. Block diagram of a comparator-based active voltage doubler to achieve higher PCE and lower dropout voltage [28].

$V_{OUT}$ is charged up to $2V_{IN,peak}$ - $V_{DS(N1)}$ - $V_{SD(P1)}$, and the total dropout voltage, $V_{Drop}$, is limited to $V_{DS(N1)}$ + $V_{SD(P1)}$. This $V_{Drop}$ is much smaller than the dropout voltage of the diode-based passive voltage doubler, $V_{GS(N)}$ + $V_{SG(P)}$, leading to higher PCE.

To maximize the PCE in active AC-DC converters, the pass transistors (e.g. $N_1$ and $P_1$ in Fig. 5) need to turn on and off at proper times at high frequency, such as 13.56 MHz in the Industrial, Scientific, and Medical (ISM) bands. If they turn on too late, the forward current conduction time, during which power is delivered from the LC-tank to the load, will be wasted. On the other hand, if the pass transistors turn off too late, reverse current flows from the load back to the LC-tank when $V_{VD} < V_{OUT}$, severely degrading the PCE.

Various comparator topologies, which optimize the timing of the active rectifier switching and maximize the PCE, have been previously reviewed in [29]. More recently, an active rectifier with cross-coupled latched comparators was proposed in [26], which utilized a pair of four-input common-gate comparators. These comparators are capacitively cross-coupled to drive the rectifying switches, reducing the reverse leakage current at 13.56 MHz. Another active rectifier in [27] used comparators with switched-offset biasing to compensate for the delays at 13.56 MHz, while maximizing the PCE. The comparator also utilized a peaking current source to reliably control the reverse current over a wide AC input range. Moreover, a high-frequency active voltage doubler was reported in [28], which used offset-control functions in its comparators to control both turn-on and turn-off timing. It achieved high PCE (~80%), while generating 64% higher output voltage than its input amplitude at 13.56 MHz

### *B. Reconfigurable AC-DC Converters*

Active rectifiers require higher peak inputs than their outputs, which may be temporarily unavailable at large coils distances ($d_{23}$) due to the weak coupling of the inductive link. On the other hand, active voltage doublers/multipliers are capable of generating higher output voltages than their inputs, but their PCEs are generally lower than that of active rectifiers with similar size of pass transistors. In order to address such limitations, adaptive reconfigurable AC-DC converters have been proposed for robust WPT through inductive links over an extended range [30], [31].

In [30], both voltage doubler (VD) and rectifier (REC) modes are integrated into a single structure, while employing low dropout active synchronous switches, leading to high PCE. Moreover, by utilizing an output voltage sensing circuit, the reconfigurable VD/REC can adaptively change its operating mode to either VD or REC depending on which one is a better choice for generating the desired output voltage. This helps the

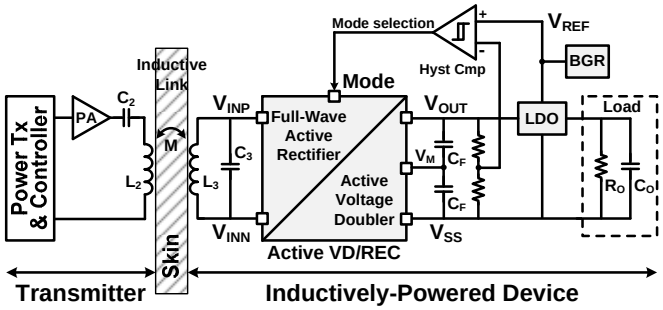


| Condition | Mode | Operation | Key Feature |
|---|---|---|---|
| $V_{OUT} > V_{REF(Hyst)}$ | 0 | Full-wave rectifier | High power efficiency (PCE) |
| $V_{OUT} < V_{REF(Hyst)}$ | 1 | Voltage doubler | High output voltage ($V_{OUT}$) |

Fig. 6. Block diagram of an inductively powered device with emphasis on the wireless power transfer through the reconfigurable VD/REC converter [30].

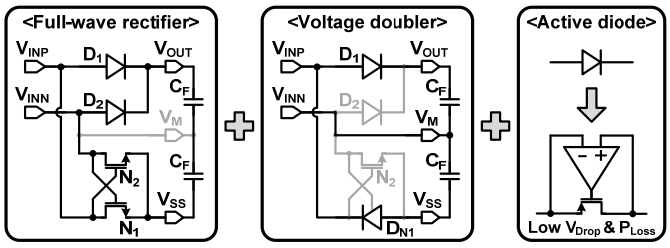


Fig. 7. Conceptual diagram of the reconfigurable VD/REC converter in which a full-wave rectifier and a voltage doubler are combined using active diodes.

VD/REC to accommodate with a wider range of coil couplings.

Figure 6 shows the block diagram of the WPT link that includes the reconfigurable VD/REC. The VD/REC converts the AC input voltage, $V_{IN} = V_{INP} - V_{INN}$, across $L_3C_3$-tank to an automatically adjusted DC voltage, $V_{OUT}$. If $V_{IN}$ falls below a certain level, which is determined by comparing a portion of $V_{OUT}$ with a reference voltage, $V_{REF}$, using a hysteresis comparator, the VD/REC operates in the VD mode (Mode = 1). Since the voltage doubler generates desired $V_{OUT}$ with much lower $V_{IN}$ than the rectifier, VD/REC can still provide sufficient $V_{OUT}$ to the load even with decreased $V_{IN}$. On the other hand, if $V_{IN}$ increases above $V_{REF}$ + hysteresis window, VD/REC will operate in the REC mode (Mode = 0) and achieve higher PCE than the VD mode while generating desired $V_{OUT}$.

The reconfigurable VD/REC can be a combination of two separate AC-DC converters, a rectifier and a voltage doubler, in which the operating mode, REC or VD, can be selected based on the input or output voltages. Figure 7 shows the conceptual diagram of the reconfigurable VD/REC converter which consists of the full-wave rectifier and the voltage doubler with active diodes. The full-wave rectifier requires two diodes, $D_1$ and $D_2$, and a cross-coupled NMOS pair, $N_1$ and $N_2$, while the voltage doubler needs only two diodes, $D_1$ and $D_{N1}$. In order for VD/REC to include both structures, $D_1$ is shared, and $D_2$ and $N_2$ have enable functions. $N_1$ operates as part of a cross-coupled pair in the REC mode, while reconfigured as an NMOS diode, $D_{N1}$, in the VD mode. $V_{INN}$ and $V_M$ are shorted through a switch in the VD mode. The VD/REC utilizes active diodes, $D_1$, $D_2$, and $D_{N1}$, which can dissipate less power than passive diodes, leading to higher PCE in both operating modes.

### *C. Hybrid AC-DC Regulators*

Despite their high PCE, the DC output voltages of the active

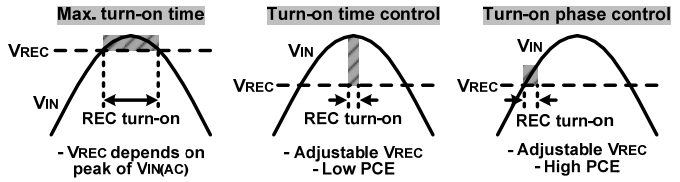


Fig. 8. Simplified voltage waveforms of the rectifiers with (a) the maximum turn-on time, (b) the turn-on time control, and (c) the turn-on phase control.

AC-DC converters are highly dependent on coil misalignments and coupling variations, which significantly affect the AC input amplitude. If eliminating these variations is left to a linear LDO, as shown in Fig. 6, it will results in additional power loss, especially when the input voltage is much higher than the desired output voltage. Recently, several researchers have proposed hybrid structures that combine the AC-DC converter and the voltage regulator. They are capable of generating a regulated output voltage through one-step adaptive AC-DC conversion, which increases the overall power efficiency, reduces the chip area, and decreases the number of large off-chip filtering capacitors [32]-[34].

Figure 8 shows the simplified voltage waveforms of the conventional and regulated AC-DC rectifiers depending on their turn-on topologies [33]. Conventional rectifiers aim to generate the maximum output voltage, $V_{REC}$, from the AC input, $V_{IN}$, at high PCE. Thus, they turn on as long as $V_{IN} > V_{REC}$, as shown in Fig. 8a. Consequently, $V_{REC}$ becomes dependent on the $V_{IN}$ amplitude, and it is not internally adjustable. In Fig. 8b, $V_{REC}$ can be adjusted by controlling the turn-on time around the peak of $V_{IN}$. If the turn-on period is reduced, the lower forward current reduces $V_{REC}$ as well. However, the large voltage drop between $V_{IN}$ and $V_{REC}$ during the turn-on period results in large power loss across the rectifying transistors, resulting in low PCE. To adjust $V_{REC}$ while maintaining high PCE, the rectifier turn-on phase can be controlled as shown in Fig. 8c. In this method, the rectifier starts turning on when $V_{IN} > V_{REC}$, similar to the conventional rectifiers. However, its turn-off timing can be controlled to limit the forward current. Therefore, $V_{REC}$ is adjustable depending on the rectifier turn-on phase, while small dropout voltage between $V_{IN}$ and $V_{REC}$ provides high PCE.

A time-controlled AC-DC converter in [32] utilized two converter cores that detect the output voltage and adjust the rectifier turn-off timing, as shown in Fig. 8c, through the comparators, digital controller, and switch drivers. Therefore, the turn-off timing is adaptively controlled by target output voltage. It needs an additional full-wave rectifier to supply the converter cores.

The adaptive regulated rectifier in [33] utilized a phase control feedback loop, which can be added to the conventional comparators to control the rectifier turn-off timing and output voltage level. It also performs comparator-based active AC-DC conversion for high PCE. Figure 9 shows the schematic diagrams of the adaptive regulated rectifier that utilizes active switches, $P_1$ and $P_2$, driven by phase control comparators, $CMP_1$ and $CMP_2$. The reference voltage, $V_{REF}$, controls the transition times of comparator output voltages, $V_{O1}$ and $V_{O2}$, in a way that the rectifier turn-off timing can be adjusted to change the turn-on phase and consequently the $V_{REC}$ level, as shown in Fig. 8c. This regulated rectifier results in small output voltage

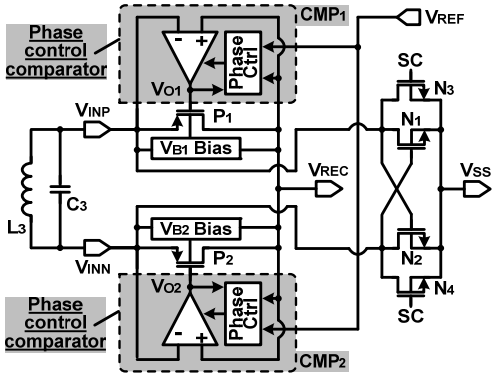


Fig. 9. Schematic diagrams of the adaptive regulated rectifier with active switches driven by phase control comparators [33].

change (< 3mV) against input amplitude variations, ensuring the line regulation capability.

More recently, a resonant regulating rectifier has been proposed in [34] for resonant wireless power transfer at 6.78 MHz. By sharing the secondary resonant coil in the inductive link, this rectifier can perform switching-mode regulation. It also employed both continuous and discontinuous conduction modes for different output power levels from 0 to 6 W.

### *D. Wireless Capacitor Chargers*

Large capacitors can be utilized as temporary energy sources and buffers to augment the wirelessly delivered power when it is interrupted or insufficient [35]. Capacitors can also be used in neural stimulation by storing charge and injecting it into the tissue periodically at high efficiency [36]. Thus, it is important to rapidly and efficiently charge capacitors in IMDs that use this mechanism directly through wireless power links. Unlike rechargeable batteries, capacitors are not constrained by specific charging profiles. Therefore, various circuit techniques can be utilized to improve capacitor charging efficiency through an inductive link.

Figure 10 shows the wireless capacitor charging system in [37], which efficiently charges positive and negative capacitor banks directly from the AC input voltage, without requiring AC-DC converters, regulators, or current sources. The $L_3C_3$-tank is followed by a series charge injection capacitor, $C_S$, providing an input voltage, $V_{IN}$, to a capacitor charger. The capacitor charger consists of switches driven by high-speed active drivers to connect $V_{IN}$ to either positive or negative capacitors. For example, when the coil voltage, $V_{COIL}$, increases and $V_{IN}$ is less than the positive capacitor voltage, the capacitor charger turns off, and $V_{IN}$ becomes floated. Thus, $V_{IN}$ also increases along with $V_{COIL}$. When $V_{IN}$ exceeds the positive capacitor voltage, the capacitor charger connects $V_{IN}$ to the positive capacitor voltage, which remains relatively constant, while $V_{COIL}$ continues increasing. Thus, the voltage variation across $C_S$ generates a positive charging current, $+I_{CH}$, for each carrier cycle to charge the positive capacitor.

The amount of $I_{CH}$ can be controlled by adjusting $C_S$, $V_{COIL}$ amplitude, and $f_p$. Charging the capacitors with fixed $I_{CH}$ can minimize switching losses in the capacitor charger. Moreover, the voltage drop across $C_S$, which operates like an ideal current source, does not dissipate power, improving the capacitor charging efficiency. As described in Fig. 1, a capacitor tuner can be utilized to compensate for the $L_3C_3$-tank resonance

TABLE I
VARIOUS AC-DC CONVERTER SPECIFICATIONS

| Publication | | 2012 [26] | 2014 [27] | 2013 [28] | 2012 [30] | | 2013 [31] | | 2010 [32] | 2013 [33] | 2013 [34] | 2013 [37] |
|---|---|---|---|---|---|---|---|---|---|---|---|---|
| Technology | | 0.18 µm CMOS | 0.35 µm CMOS | 0.5 µm CMOS | 0.5 µm CMOS | | 0.35 µm CMOS | | 0.18 µm CMOS | 0.5 µm CMOS | 0.35 µm BCD | 0.35 µm CMOS |
| Structure | | Active rectifier | Active rectifier | Active voltage doubler | Reconfigurable VD/REC | | Reconfigurable 1× / 2× | | AC-DC regulator | AC-DC regulator | AC-DC regulator | Wireless capacitor charger |
| | | | | | REC | VD | 1× | 2× | | | | |
| $V_{IN,peak}$ (V) | | 1.5 | 1.5 ~ 4 | 1.46 | 3.7 | 2.15 | 1.5 ~ 4 | 1.2 ~ 2.5 | 3.5 | 5 | N/A | 2.7 |
| $V_{OUT}$ (V) | | 1.33 | 1.19 ~ 3.52 | 2.4 | 3.1 | 3.1 | 1.27 ~ 4 | | 1.25 ~ 2 | 2.5 ~ 4.6 | 5 | ±1 ~ ±2 |
| VCE (%)* | | 89 | 79 ~ 89 | 82.2 | 83.8 | 72.1 | 85 ~ 90 | 65 ~ 80 | 36 ~ 57 | 50~92 | N/A | 37 ~ 74 |
| $R_O$ (kΩ)** | | 1 | 0.5 | 1 | 0.5 | | 0.5 | | $P_L$ = 4mW | $I_L$ = 2.8mA | $P_L$ = 3.4W | Cap = 1µF |
| $f_p$ (MHz) | | 13.56 | 13.56 | 13.56 | 13.56 | | 13.56 | | 1 | 2 | 6.78 | 2 |
| Area (mm$^2$) | | 0.009 | 0.186 | 0.144 | 0.585 | | 1.42 | | 0.1 | 0.3 | 5.52 | 2.1 |
| PCE (%) | Sim. | N/A | 84.2 ~ 90.7 | 80 | 81 | 75 | N/A | N/A | N/A | 78 ~ 94 | N/A | 77 ~ 88 |
| | Meas. | 81.9 | 82.2 ~ 90.1 | 79 | 77 | 70 | 81 ~ 84 | 61 ~ 76 | 68 ~ 90 | 72 ~ 87 | 55 | 63 ~ 82 |

* Voltage conversion efficiency (VCE) = $V_{OUT}$ / ($V_{IN,peak}$ × multiplication factor), ** DC load resistance after the power management unit.

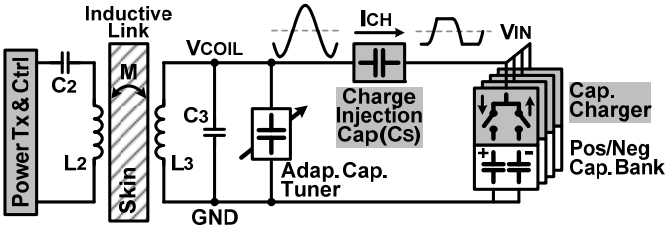


Fig. 10. Wireless capacitor charging system through an inductive link [37].

capacitance variations during charging period to maintain $V_{COIL}$ amplitude constant at its peak.

A wireless capacitor charger in [38] aims for rapid charging through the inductive link. It utilizes a three-tap secondary coil and its control system to modify secondary inductance and resonant capacitance, which can adjust the optimal load impedance for the link. This enables the maximum power delivery with dynamically-optimized load impedance during capacitor charging interval, minimizing charging time. Table I summarizes the specifications of various AC-DC converters, regulators, and chargers introduced in this section.

## IV. LOW-POWER WIRELESS DATA TELEMETRY (WDT)

Sending data wirelessly from the external unit to the IMD is known as the forward telemetry while dataflow in the opposite direction is often referred to as back telemetry.

### A. Single-Carrier Forward/Back Data Telemetry

A simple option for forward/back telemetry, which has been used in most of todays' IMDs, is modulation of the power carrier for transmitting data. For forward telemetry, amplitude shift keying (ASK) has been popular in the past because of its simple modulation and demodulation circuitry [39]. This method, however, is not robust against inductive coupling variations, which motivates the use of frequency and phase shift keying (FSK and PSK). A phase-coherent FSK was proposed in [40] to increase the data rate to 2.5 Mbps. However, this method occupies a wide bandwidth (> 5 MHz), which is not available in high-Q inductive links. A few groups have developed circuits based on binary and quadrature PSK [41], [42], which require smaller bandwidth compared to FSK.

The conventional method for back telemetry is called load shift keying (LSK), which is similar to the backscattering method in RFID tags, good for data rates up to 0.5 Mbps [43]. An improved LSK method has also been proposed in [44] to increase the data rate to 2.8 Mbps. However, LSK requires strong coupling between the coils, and it entirely shuts off the power transfer to the IMD during the data transmission periods.

### B. Multi-Carrier Data Telemetry

The main advantage of using a single carrier for both power and data transmission is the relatively robust coupling between power coils, which can lead to more reliable data transfer. Another advantage is the space saving by reusing power coils for data transmission. In high-performance IMDs that require wider bandwidth, however, separating power carrier from the data carrier is desired because increasing the frequency of the strong power carrier can cause interference and safety issues due to excessive power loss in the tissue. To achieve high PTE and high data rate, a high frequency data carrier, $f_d$ > 50 MHz, is required for the data link while $f_p$ can be kept below 20 MHz [11]. This has led to the use of dual-carrier power/data links as shown in Fig. 11a with each carrier linking a separate pair of coils [45]-[47].

A major challenge in dual-carrier designs is the cross-couplings between the two pairs of power and data coils, which need to be miniaturized as they are housed inside the small IMD. In particular, the strong power carrier interference can dwarf the weak data signal on the Rx side and make data recovery quite difficult. In other words, to achieve a low bit-error-rate (BER), a large signal-to-interference ratio (SIR) is needed in the data Rx. While several innovative coil designs have helped with reducing the coils' cross couplings [48]-[50], it is still necessary to filter out the power carrier interference at the Rx input electronically [51].

The data carrier has recently been substituted with a series of narrow pulses in near-field, similar to far-field impulse radio ultra-wideband (IR-UWB), to further reduce the data Tx power consumption and increase the data rate [52]. In order to reduce the inter-symbol interference (ISI), however, the bandwidth of the Rx LC-tank has been increased by reducing its Q-factor that makes it highly vulnerable to the power carrier interference.

In order to achieve high data rates with a high-Q LC-tank on the Rx side, Pulse Harmonic Modulation (PHM) has been proposed in [53], sending a series of sharp pulses, which timing and amplitude have been carefully selected to reduce the ISI in the Rx coil. To transmit each bit "1", the PHM Tx generates a sharp pulse at the onset of the bit period to initiate a ringing

TABLE II
BENCHMARKING OF INDUCTIVE TELEMETRY LINKS

| Publication | 2004 [40] | 2005 [41] | 2008 [44] | 2010 [45] | 2012 [46] | 2012 [46] | 2008 [47] | 2013 [51] | 2013 [55] | 2015 [56] |
|---|---|---|---|---|---|---|---|---|---|---|
| CMOS Tech. (μm) | 1.5 | 0.18 | 0.5 | - | 0.8 | 0.8 | 0.35 | 0.18 | 0.35 | 0.35 |
| Modulation | pcFSK | BPSK | LSK | QPSK | FSK | BPSK | BPSK | DPSK | PHM | PDM |
| Distance (mm) | 5 | 15 | 20 | 5 | 20 | 20 | 10 ~ 15 | - | 10 | 10 |
| $f_d$ and $f_p$ (MHz) | 5/10 | 10 | 25 | 13.56 & 1 | -/5 & 5 | 48 & 5 | 20 & 2 | 20 & 2 | 66.5& - | 50 & 13.56 |
| Data Rate (Mbps) | 2.5 | 1.12 | 2.8 | 4.16 | 1.25 | 3 | 2 | 2 | 20 | 13.56 |
| Tx/Rx Power Cons. (pJ/bit) | -/152 | -/625 | 35.7/1250 | - | - | 1962/- | -/3100 | - | 345/294 | 960/162 |
| SIR (dB) | - | - | - | - | - | - | -12* | - | - | -18.5 |
| Tx/Rx Area (mm$^2$) | -/0.29 | -/0.2 | 2.2/2.2 | - | - | 2.3 | -/4.4 | - | 0.1/0.5 | 0.34/0.37 |
| BER | $10^{-5}$ | $10^{-5}$ | $10^{-6}$ | $2\times10^{-6}$ | - | $2\times10^{-4}$ | $10^{-7}$ | $10^{-7}$ | $8.7\times10^{-7}$ | $4.3\times10^{-7}$ |

* A first order off-chip filter was used to improve SIR to -6 dB.

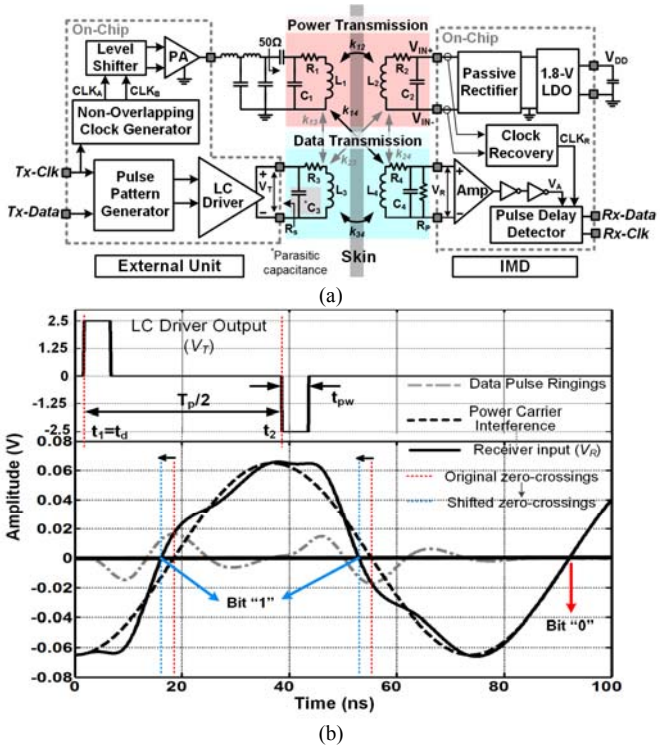


Fig. 11. (a) Block diagram of a dual-band inductive power and data transmission link using the PDM scheme. (b) PDM operational waveforms.

response in the high-Q Rx LC-tank. A second pulse is then generated with specific amplitude and delay with respect to the initial pulse that suppresses the residual ringing across the Rx LC-tank to expedite the end of the bit period. No pulses are transmitted in this scheme for bit "0". This method allows for reaching high data rates in excess of 10 Mbps without reducing the inductive link Q-factor, which helps to extend the range and reject the power carrier interference to some extent [54], [55]. However, PHM operates only when the SIR at Rx input is sufficient, i.e. SIR > 0 dB.

Recently, a new carrier-less data transmission scheme, called Pulse Delay Modulation (PDM), has been developed for simultaneous data and power transmission [56]. The novel aspect in the PDM is the utilization of undesired power carrier interference across the Rx input to deliver the data bits even with SIR < 0 dB. Figure 11a shows a PDM-based link, in which two separate links are used for power ($L_1$-$L_2$) and data ($L_3$-$L_4$) transmission. In the presence of narrow pulses across $L_3C_3$-tank for data bit "1", a ringing appears across the low-Q $L_4C_4$-tank due to $k_{34}$ at the resonance frequency of the tank, $f_d$, as shown in dashed gray in Fig. 11b. Without data pulse ringing, the induced power carrier interference across $L_4C_4$-tank is a clean sinusoid, shown by the dashed black waveform in Fig. 11b. The actual received signal, $V_R$ shown in solid black, however, results from the superposition of the data and power components. PDM has successfully shifted the zero-crossing times of the superimposed waveform, $V_R$, for a bit "1", which can be easily detected on the Rx side. The PDM transceiver in Fig. 11a has achieved a data rate of 13.56 Mbps with a BER of $4.3\times10^{-7}$ across a 10 mm inductive link, while the power link has delivered 42 mW of regulated power to the load at the same frequency. Table II compares different methods for inductive power and data transmission.

## V. CONCLUSION

Various wireless power and data transmission techniques that can be utilized to power up and communicate with IMDs and other appliances in the near-field have been reviewed. The wireless power transfer consists of several stages, such as the power Tx, wireless link, matching circuit, and power conversion/management unit. Every stage offers the designer with several degrees of freedom and design parameters, which need to be optimally combined by considering specifications in a designated application, such as power efficiency, supply voltage level, coupling distance, delivered power capacity, operating frequency, coil misalignments, and device size. In addition, low-power and robust wireless data telemetry (WDT) in the presence of power interference becomes important in information-centric IMDs, in which high performance is desired but the received power is limited. Several efficient WDT techniques have been introduced, which can be adopted to handle wideband bidirectional communication with IMDs.

## REFERENCES


[1] M. Rasouli and L.S.J. Phee, "Energy sources and their development for application in medical devices," *Expert Review of Medical Devices*, vol. 7, no. 5, pp. 693-709, Sep. 2010.

[2] L. D. Cruz, et al, "The Argus II epiretinal prosthesis system allows letter and word reading and long-term function in patients with profound vision loss," *Br. J. Ophthalmol*. Feb. 2013.

[3] A. V. Nurmikko, et al, "Listening to brain microcircuits for interfacing with external world-progress in wireless implantable microelectronic neuro-engineering devices," *Proc. IEEE*, vol. 98, pp. 375-388, Mar. 2010.

[4] M. Ghovanloo, "Integrated circuits for neural interfacing: Neural stimulation," in *VLSI Circuits for Biomedical Applications*, K. Iniewski, Ed. Norwood, MA: Artech House, 2008.

[5] S. Haddad, R. Houben, and W. Serdijn, "The evolution of pacemakers," *IEEE Eng. Med. Biol. Magazine*, vol. 25, pp. 38-48, May 2006.

[6] G. Lazzi, "Thermal effects of bioimplants," *IEEE Eng. Med. Biol. Mag.*, vol. 24, no. 5, pp.75 -81, Sep. 2005.

[7] M. Catrysse, B. Hermans, and R. Puers, "An inductive power system with integrated bidirectional data-transmission," *Sens. Actuators A*, vol. 115, pp. 221-229, Sep. 2004.

[8] T. Fujii and Y. Ibata, "Effects of heating on electrical activities of guinea pig olfactory cortical slices," *Eur. J. Physiol.* vol. 392, pp. 257-260, 1982.

[9] K. Chen, et al, "An integrated 256-channel epiretinal prosthesis," *J. Solid State Circuit*, vol. 45, pp. 1946-1956, Sept. 2010.

[10] R. Normann, "Technology insight: future neuroprosthetic therapies for disorders of the nervous system," *Nature Clinical Practice*, vol. 3, pp. 444-452, Aug. 2007.

[11] M. Ghovanloo and S. Atluri, "A wideband power-efficient inductive wireless link for implantable microelectronic devices using multiple carriers," *IEEE Trans. Circuit Syst. I*, vol. 54, pp. 2211-2221, Oct. 2007.

[12] FCC Rules and Regulations, *MICS Band Plan*, Part 95, 2003.

[13] M. W. Baker and R. Sarpeshkar, "Feedback analysis and design of RF power links for low-power bionic systems," *IEEE Trans. Biomed. Cir. Syst.*, vol. 1, no. 1, pp. 28-38, Mar. 2007.

[14] A. Kurs, et al, "Wireless power transfer via strongly coupled magnetic resonances," *Science Express*, vol. 317, pp. 83-86, Jul. 2007.

[15] A. Karalis, J. Joannopoulos, and M. Soljacic, "Efficient wireless nonradiative mid-range energy transfer," *Ann. Phys.*, vol. 323, pp. 34-48, Apr. 2007.

[16] M. Kiani, U. Jow, and M. Ghovanloo, "Design and optimization of a 3-coil inductive link for efficient wireless power transmission," *IEEE Trans. Biomed. Cir. Syst.*, vol. 5, pp. 579-591, Dec. 2011.

[17] M. Kiani and M. Ghovanloo, "The circuit theory behind coupled-mode magnetic resonance based wireless power transmission," *IEEE Trans. Circuits Syst. I*, vol. 59, Sept. 2012.

[18] R. Xue, K. Cheng, and M. Je, "High-efficiency wireless power transfer for biomedical implants by optimal resonant load transformation," *IEEE Trans. Biomed. Cir. Syst.*, vol. 60, pp. 867-874, Apr. 2013.

[19] K. Silay, et al, "Load optimization of an inductive power link for remote powering of biomedical implants," in Proc. *IEEE Int. Symp. Cir. Syst.*, pp. 533-536, May 2005.

[20] M. Zargham and P. Gulak, "Maximum achievable efficiency in near-field coupled power-transfer systems," *IEEE Trans. Biomed. Cir. Syst.*, vol. 6, pp. 228-245, Jun. 2012.

[21] M. Kiani, B. Lee, P. Yen, and M. Ghovanloo, "A power management ASIC with Q-modulation capability for efficient inductive power transmission," *IEEE Intl. Solid-State Cir. Conf.*, pp. 226-227, Feb. 2015.

[22] J.V. Ham and R. Puers, "A power and data front-end IC for biomedical monitoring systems," *Sens. Actuators A*, vol. 147, pp. 641-648, Oct. 2008.

[23] C. Sauer, M. Stanacevic, G. Cauwenberghs, and N. Thakor, "Power harvesting and telemetry in CMOS for implanted devices," *IEEE Trans. Circuits Syst. I*, vol. 52, no. 12, pp. 2605-2613, Dec. 2005.

[24] F. Mounaim and M. Sawan, "Integrated high-voltage inductive power and data-recovery front end dedicated to implantable devices," *IEEE Trans. Biomed. Circuits Syst*., vol. 5, no. 3, pp. 283–291, Jun. 2011.

[25] J. Yoo, L. Yan, S. Lee, Y. Kim, and H. Yoo, "A 5.2mW self-configured wearable body sensor network controller and a 12μW 54.9% efficiency wirelessly powered sensor for continuous health monitoring system," *IEEE J. Solid-State Circuits*, vol. 45, no. 1, pp. 178-188, Jan. 2010.

[26] H. Cha, W. Park, and M. Je, "A CMOS rectifier with a cross-coupled latched comparator for wireless power transfer in biomedical applications," *IEEE Trans. Cir. Syst. II*, vol. 59, pp. 409-413, Jul. 2012.

[27] Y. Lu and W. Ki, "A 13.56 MHz CMOS active rectifier with switched-offset and compensated biasing for biomedical wireless power transfer systems," *IEEE Trans. Biomed. Cir. Syst.*, vol. 8, pp. 334-344, Jun. 2014.

[28] H.-M. Lee and M. Ghovanloo, "A high frequency active voltage doubler in standard CMOS using offset-controlled comparators for inductive power transmission," *IEEE Trans. Biomed. Circuits Syst.*, vol. 7, no. 3, pp. 213-224, Jun. 2013.

[29] H.-M. Lee and M. Ghovanloo, "Fully integrated power-efficient AC-to-DC converter design in inductively-powered biomedical applications," in *Proc. IEEE Custom Integrated Circuits Conference (CICC)*, Sep. 2011.

[30] H.-M. Lee and M. Ghovanloo, "An adaptive reconfigurable active voltage doubler/rectifier for extended-range inductive power transmission," *IEEE Trans. Circuits Syst. II,* vol. 59, no. 8, pp. 481-485, Aug. 2012.

[31] Y. Lu, X. Li, W.-H. Ki, C.-Y. Tsui, and C. P. Yue, "A 13.56MHz fully integrated 1x/2x active rectifier with compensated bias current for inductively powered devices," in *IEEE Int. Solid-State Cir. Conf.*, pp. 66-67, Feb. 2013.

[32] K. F. E. Lee, "A timing controlled AC-DC converter for biomedical implants," in *IEEE Int. Solid-State Cir. Conf.*, pp. 128-129, Feb. 2010.

[33] H.-M. Lee, H. Park, and M. Ghovanloo, "A power-efficient wireless system with adaptive supply control for deep brain stimulation," *IEEE J. Solid-State Circuits*, vol. 48, no. 9, pp. 2203-2216, Sep. 2013.

[34] J. Choi, S. Yeo, S. Park, J. Lee, and G. Cho, "Resonant regulating rectifiers (3R) operating for 6.78 MHz resonant wireless power transfer (RWPT)," *IEEE J. Solid-State Cir.*, vol. 48, pp. 2989-3001, Dec. 2013.

[35] U. Jow, M. Kiani, X. Huo, and M. Ghovanloo, "Towards a smart experimental arena for long-term electrophysiology experiments," *IEEE Trans. Biomed. Circuits Syst.*, vol. 6, no. 5, pp. 414-423, Oct. 2012.

[36] S. Kelly and J. Wyatt, "A power-efficient neural tissue stimulator with energy recovery," *IEEE Trans. Biomed. Cir. Syst.*, vol. 5, pp. 20-29, Feb. 2011.

[37] H.-M. Lee and M. Ghovanloo, "A power-efficient wireless capacitor charging system through an inductive link," *IEEE Trans. Circuits Syst. II*, vol. 60, no. 10, pp. 707–711, Oct. 2013.

[38] P. P. Mercier and A. P. Chandrakasan, "Rapid wireless capacitor charging using a multi-tapped inductively-coupled secondary coil," *IEEE Trans. Circuits Syst. I,* vol. 60, no. 9, pp. 2263-2272, Sep. 2013.

[39] R. R. Harrison, et al, "Wireless neural recording with single low-power integrated circuit," *IEEE Trans. Neural Syst. Rehabil. Eng.*, vol. 17, pp. 322-329, Aug. 2009.

[40] M. Ghovanloo and K. Najafi, "A wideband frequency-shift keying wireless link for inductively powered biomedical implants," *IEEE Trans. Circuits Syst. I*, vol. 51, no. 12, pp. 2374-2383, Dec. 2004.

[41] Y. Hu and M. Sawan, "A fully integrated low-power BPSK demodulator for implantable medical devices," *IEEE Trans. Cir. Syst. I, Reg. Papers*, vol. 52, no. 12, pp. 2552–2562, Dec. 2005.

[42] Z. Lu and M. Sawan, "An 8 Mbps data rate transmission by inductive link dedicated to implantable devices," in *Proc. IEEE Int. Symp. Cir. Syst.*, pp. 3057-3060.

[43] D. Paret*, RFID and Contactless Smart Card Applications*. Hoboken, NJ: Wiley, 2005.

[44] S. Mandal and R. Sarpeshkar, "Power-efficient impedance-modulation wireless data links for biomedical implants," *IEEE Trans. Biomed. Cir. Syst.*, vol. 2, pp. 301-315, Dec. 2008.

[45] G. Simard, M. Sawan, D. Massiocotte, "High-speed OQPSK and efficient power transfer through inductive link for biomedical implants," *IEEE Trans. Biomed. Cir. Syst.*, vol. 4, no. 3, pp. 192-200, Jun. 2010.

[46] A. Rush and P. Troyk, "A power and data link for a wireless-implanted neural recording system," *IEEE Trans. Biomed. Cir. Syst.*, vol. 59, pp. 3255-3262, Nov. 2012.

[47] M. Zhou, M. Yuce, and W. Liu, "A non-coherent DPSK data receiver with interference cancellation for dual-band transcutaneous telemetries," *IEEE J. Solid-State Circuits*, vol. 43, no. 9, pp. 2003–2012, Sep. 2008.

[48] U. Jow and M. Ghovanloo, "Optimization of data coils in a multiband wireless link for neuroprosthetic implantable devices," *IEEE Trans. Biomed. Cir. Syst.*, vol. 4, no. 5, pp. 301–310, Oct. 2010.

[49] G. Wang, P. Wang, Y. Tang, and W. Liu, "Analysis of dual band power and data telemetry for biomedical implants," *IEEE Trans. Biomed. Cir. Syst.*, vol. 6, pp. 208-215, June 2012.

[50] G. Simard, M. Sawan, and D. Massicotte, "Novel coils topology intended for biomedical implants with multiple carrier inductive link," *IEEE Int. Symp. Cir. Syst.*, pp. 537-540, May 2009.

[51] K. Chen, Y. Lo, and W. Liu, "A 37.6mm2 1024-channel high-compliance-voltage SoC for epiretinal prostheses," *IEEE Intl. Solid-State Cir. Conf.*, pp. 294-295, Feb. 2013.

[52] S. Lee, K. Song, J. Yoo, and H. Yoo, "A low-energy inductive coupling transceiver with cm-range 50-Mbps data communication in mobile device applications," *IEEE J. Solid-State Cir.*, vol. 45, pp. 2366-2374, Nov. 2010.

[53] F. Inanlou and M. Ghovanloo, "Wideband near-field data transmission using pulse harmonic modulation," *IEEE Trans. Circuits Syst. I*, vol. 58, no. 1, pp. 186–195, Jan. 2011.

[54] F. Inanlou, M. Kiani, and M. Ghovanloo, "A 10.2 Mbps pulse harmonic modulation based transceiver for implantable medical devices," *IEEE J. Solid-State Cir.*, vol. 46, pp.1296-1306, June 2011.

[55] M. Kiani and M. Ghovanloo, "A 20 Mbps pulse harmonic modulation transceiver for wideband near-filed data transmission," *IEEE Trans. Circuits Syst. II*, vol. 60, pp. 382-386, July 2013.

[56] M. Kiani and M. Ghovanloo, "A 13.56-Mbps pulse delay modulation based transceiver for simultaneous near-field power and data transmission," *IEEE Trans. Biomed. Cir. Syst.*, vol. 9, pp. 1-11, Feb. 2015.